nature energy

SUPPLEMENTARY INFORMATION

https://doi.org/10.1038/s41560-017-0068-x

In the format provided by the authors and unedited.

Spatial decoupling of light absorption and catalytic activity of Ni–Mo-loaded high-aspect-ratio silicon microwire photocathodes

Wouter Vijselaar[1], Pieter Westerik[2], Janneke Veerbeek[1], Roald M. Tiggelaar[2,3], Erwin Berenschot[2], Niels R. Tas[2], Han Gardeniers[2]* and Jurriaan Huskens[1]*

[1]Molecular NanoFabrication, MESA+ Institute for Nanotechnology, University of Twente, Enschede, The Netherlands. [2]Mesoscale Chemical Systems, MESA+ Institute for Nanotechnology, University of Twente, Enschede, The Netherlands. [3]NanoLab Cleanroom, MESA+ Institute for Nanotechnology, University of Twente, Enschede, The Netherlands. *e-mail: j.g.e.gardeniers@utwente.nl; j.huskens@utwente.nl

Supporting Information

Spatial Decoupling of Light Absorption and Catalytic Activity of Ni-Mo-Loaded High-Aspect-Ratio Silicon Microwire Photocathodes

Wouter Vijselaar, Pieter Westerik, Janneke Veerbeek, Roald M. Tiggelaar, Erwin Berenschot, Niels R. Tas, Han Gardeniers, Jurriaan Huskens

Supplementary Figures

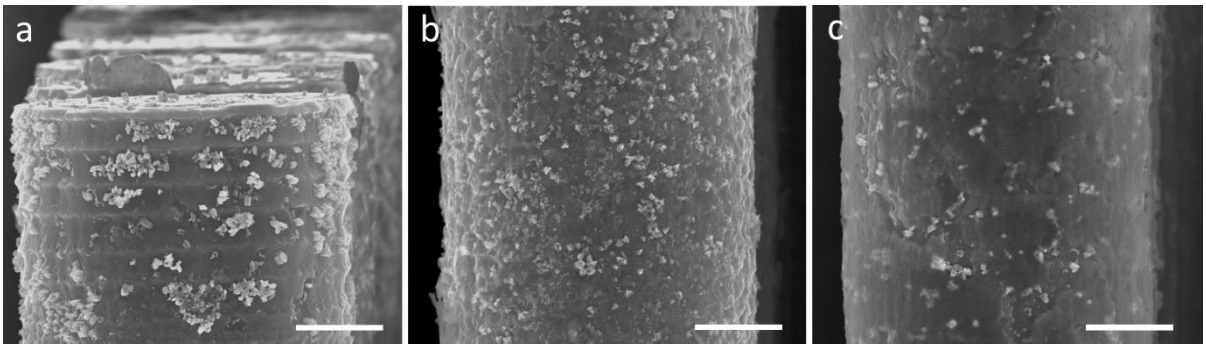

Supplementary Figure 1. HR-SEM images from (**a**) top, (**b**) middle, and (**c**) bottom section of a single micropillar which was completely exposed to 30 s electrodeposition of Ni-Mo (30 s) (see main text, sample a, Figure 1d). Scale bar is set to 1 µm.

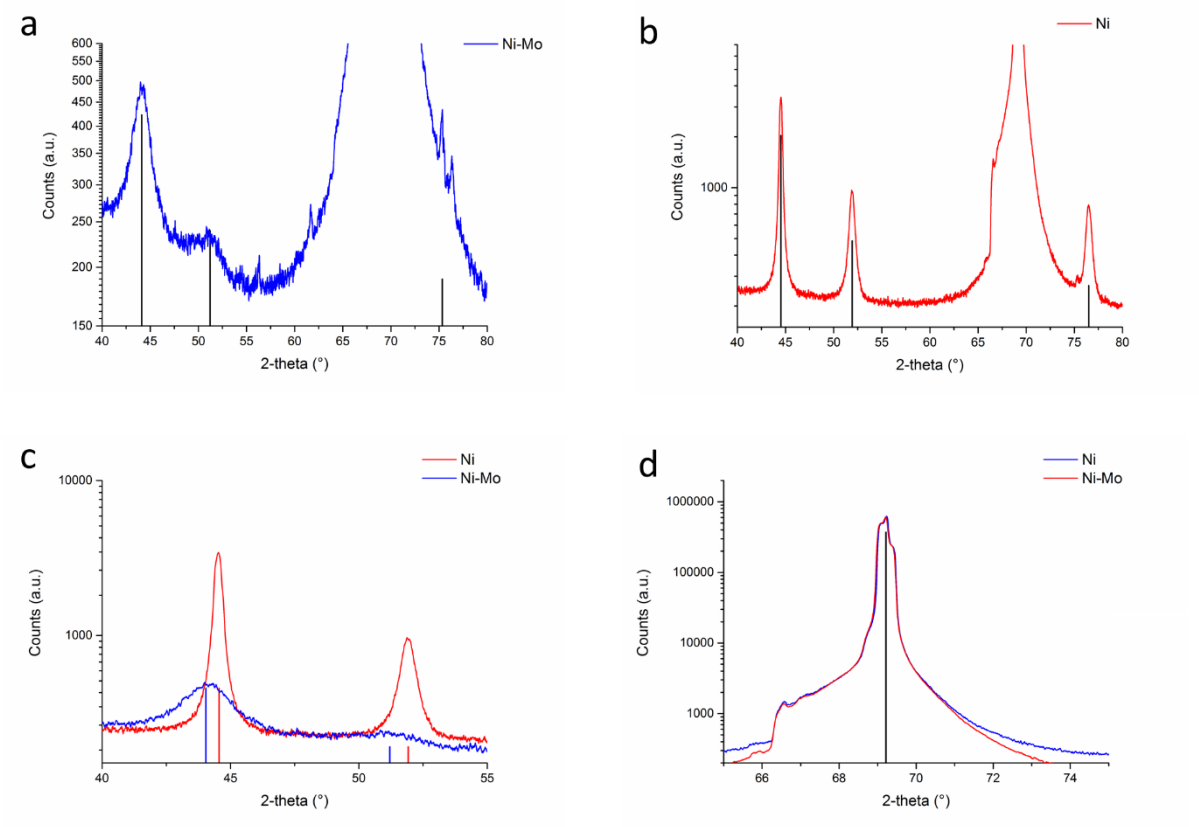

Supplementary Figure 2. XRD patterns of electrodeposited nickel (30 s) and alloyed nickel molybdenum films on flat silicon, with their characteristic peaks and relative intensities marked. (**a**) Ni/Si,[1] (**b**) Ni-Mo/Si,[2] (**c**) an overlap of the Ni and Ni-Mo pattern, and (**d**) an overlap of the Si peak in each pattern. Supplementary Figure 2a shows the XRD pattern of 30 s electrodeposited Ni on a flat Si, here the (111), (002), and (022) peaks are observed at 44.56°, 51.92°, and 76.50°, respectively and no interfacial phases.[1] The high intensity peak at 69.13° is p-Si (400). Supplementary Figure 2b shows the XRD pattern of 180 s electrodeposited Ni-Mo on flat Si. The (111), (002) and (022) peaks of Ni-Mo are at 43.96°, 51.21°, and 75.35°, respectively, and the (400) peak of Si is at 69.13°.[2] The shift of the peaks is clearly visualized in the combined XRD pattern of Supplementary Figure 2c, which confirms the incorporation of Mo atoms in the nickel structure. To confirm the alignment of the XRD apparatus, a combined graph of the Si signals is given in Supplementary Figure 2d, where no shift is observed between the Si signals of the two different Si substrates.[2]

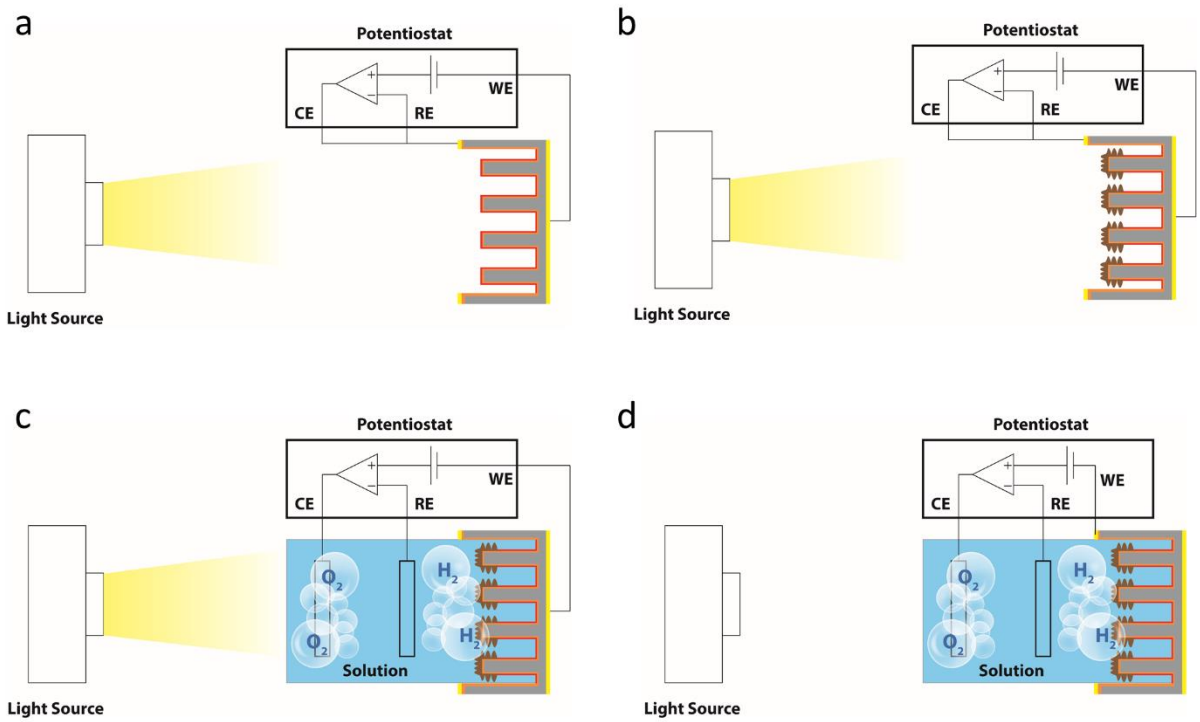

Supplementary Figure 3. (**a**) Schematic overview of the light JV measurement setup for fully passivated microwire PV cells. (**b**) Schematic overview of the light JV measurement setup for spatioselectively catalyst-functionalized microwire PV cells. (**c**) Schematic overview of the light JE measurement setup for spatioselectively catalyst-functionalized microwire photocathodes. (**d**) Schematic overview of the dark JV measurement setup. Supplementary Figure 3 gives a schematic representation of how the potentiostat is connected to the samples to measure specific elements of the photocathode. CE is the counter electrode, RE is the reference electrode, and WE is the working electrode. Supplementary Figure 3a and b shows a schematic setup used to measure the JV characteristics of the underlying PV cell. A sample is placed at 1 sun intensity (see Methods for calibration details) and scanned by a linear scan between -0.7 and 0.7 V. The difference between Supplementary Figure 3a and b is only the use of a “bare” (passivated) sample or with catalyst. Note that the RE and CE are connected together at the front side and that the WE is connected at the backside. Supplementary Figure 3c is a schematic representation of the setup used to measure a HER half-cell. The sample again is placed at 1 sun intensity, at the same position as the samples in Supplementary Figure 3a and b. The CE is a Pt mesh in a circle around the sample, in order not to intervene with the light. The RE is a Ag/AgCl electrode, which is placed in close proximity of the sample. The WE is connected at the backside. Supplementary Figure 3d is a schematic representation of the setup used to measure the catalytic activity of the electrodeposited catalyst. The CE and RE are used in the same manner as in Supplementary Figure 3c, but the WE is connected to the frontside of the sample. In this manner we by-pass the p/n junction and we can measure the activity of the catalyst.

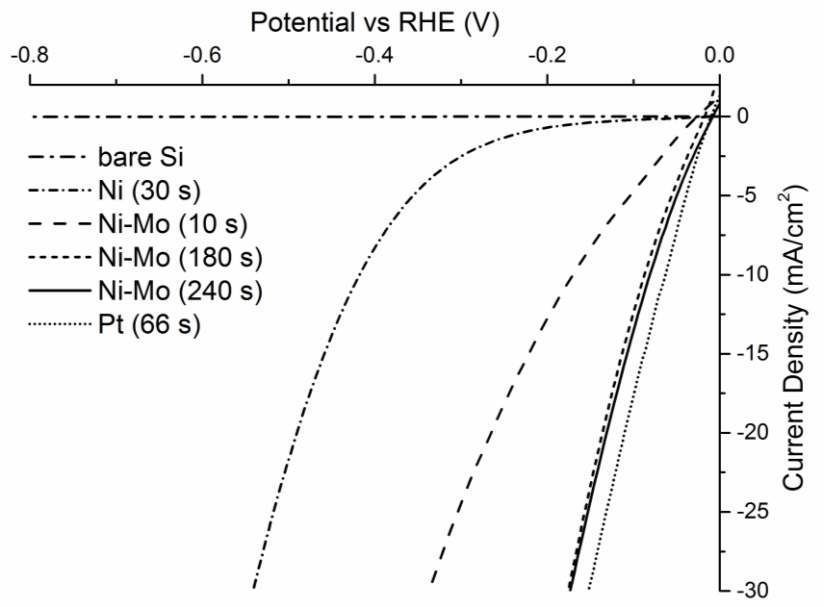

Supplementary Figure 4. Dark *JE* behavior for electrodes with the noted compositions. The Si micropillars were radially doped (n^+/p) and in this case completely covered with the noted catalyst (sample a). All samples were evaluated in 0.1 M H_2SO_4(aq). Supplementary Figure 4 shows the dark *JE* measurements for HER electrocatalysis on n^+-Si micropillar array substrates, without or completely covered with a catalyst of Ni, Ni-Mo and Pt (sample a). The used setup to measure the activity is given in Supplementary Figure 3d. The band edge position of Si straddles the H^+/H_2 redox couple, and almost no catalytic activity is observed over a large overpotential range for bare Si micropillars, which underlines the requirement for a catalyst. The addition of a smooth, continuous Ni film on the surface already improves the catalytic activity substantially (Ni (30 s)). A relatively small addition of Na_2MoO_4 (<2 mol% Mo to Ni) to the plating bath solution increases the HER activity in an acidic environment even more. Such a Ni-Mo alloy on n^+-Si micropillar arrays gives *JE* responses that exhibit increasing catalytic activities with increasing deposition time. Increasing the deposition times beyond 180 s does not have any further effect, as is seen by increasing the deposition time to 240 s. Furthermore these layers show a catalytic activity similar to that of Pt.

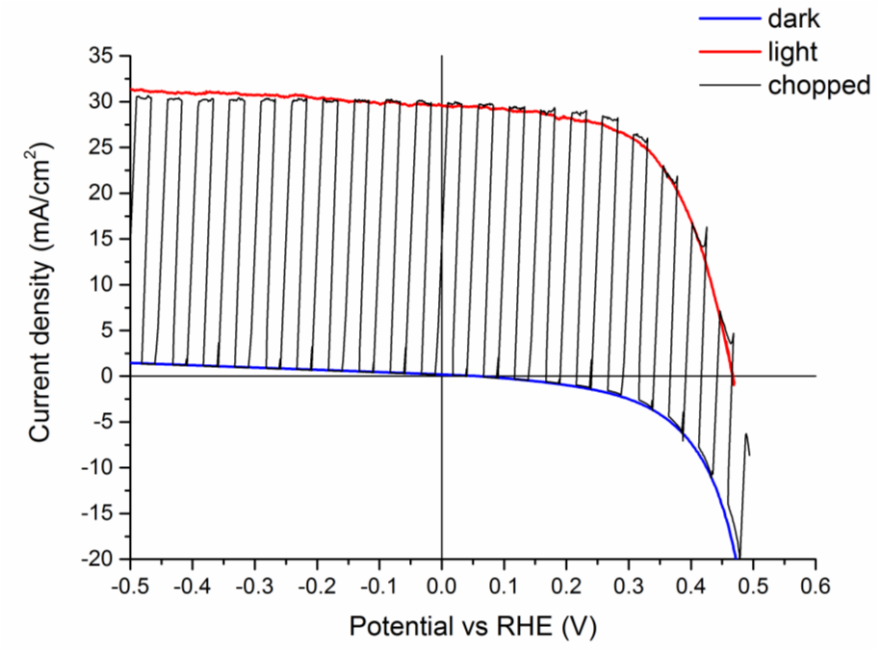

Supplementary Figure 5. Current density J_{ph} versus potential (E) behavior of Si micropillar array devices with radial n^+/p-junctions with electrodeposited Ni-Mo solely at the tops of Si micropillars (sample b) in dark and in both chopped simulated sunlight and continuous simulated sunlight. The used setup to measure the activity is given in Supplementary Figure 3c.

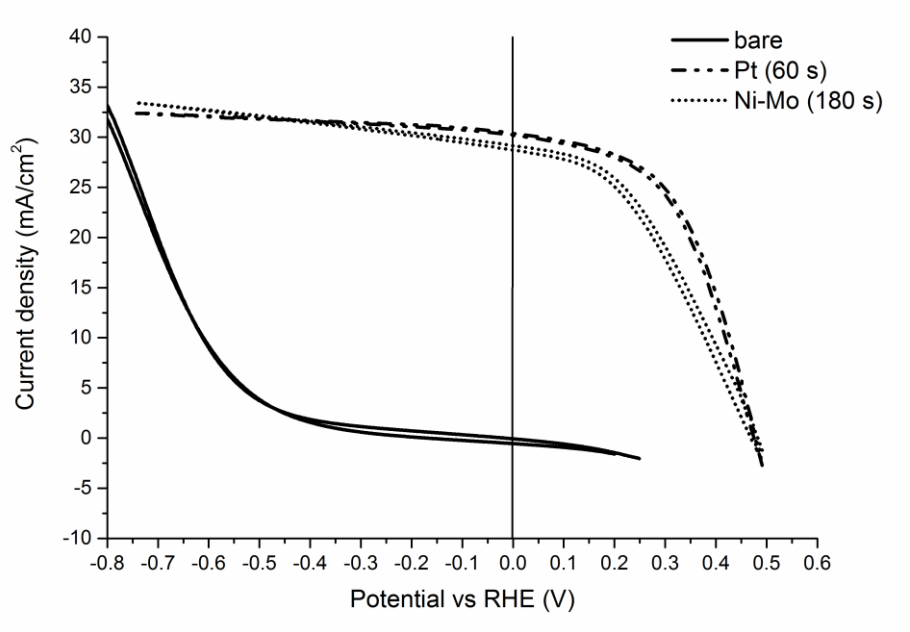

Supplementary Figure 6. Current density J_{ph} versus potential (E) behaviour of Si micropillar array devices with radial n^+/p-junctions with electrodeposited Pt or Ni-Mo solely at the tops of Si micropillars. Here, the x and y-axes are extended to show we do not cross over into the oxidative regime with the measured CV scans. The used setup to measure the activity is given in Supplementary Figure 3c.

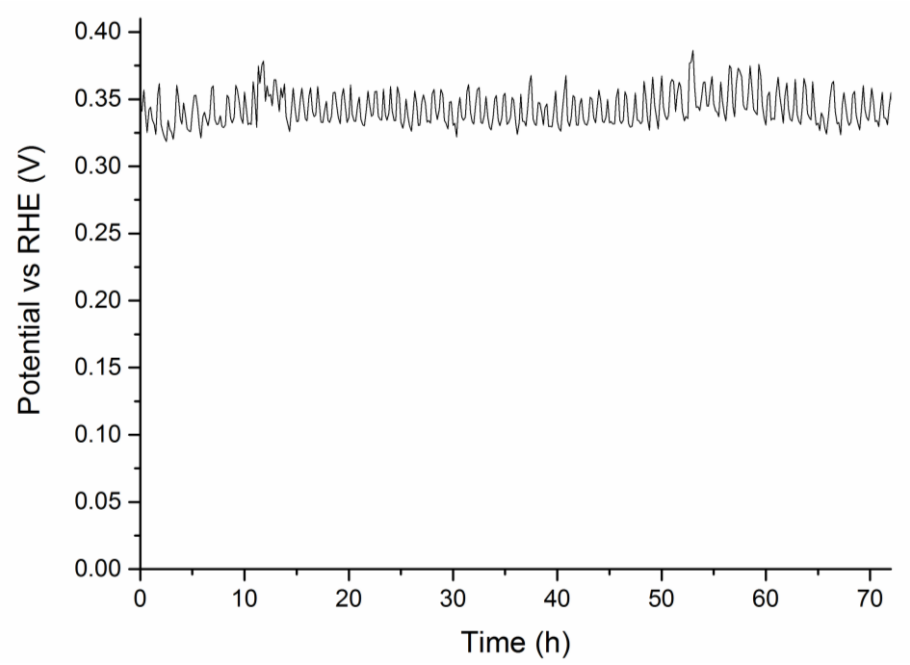

Supplementary Figure 7. Recorded potential of a spatioselectively deposited Ni-Mo catalyst on Si micropillars under continuous operation of 10 mA/cm^2 and AM 1.5G simulated sunlight. Microwire array with 6 µm pitch, upper 2 µm functionalized with Ni-Mo (180 s deposition). The used setup to measure the activity is given in Supplementary Figure 3c. As noted, Ni-Mo does not exhibit infinite stability under strong acidic conditions.[3] To assess the durability of this catalyst we measured the potential vs RHE at a constant current density of 10 mA/cm^2 in a buffered (pH 4.0) electrolyte of 0.2 M potassium hydrogen phthalate for 72 h under AM 1.5G light. The average recorded potential appeared stable over the entire period of time, and the potential only oscillated, most probably due to hydrogen bubble formation and detachment.

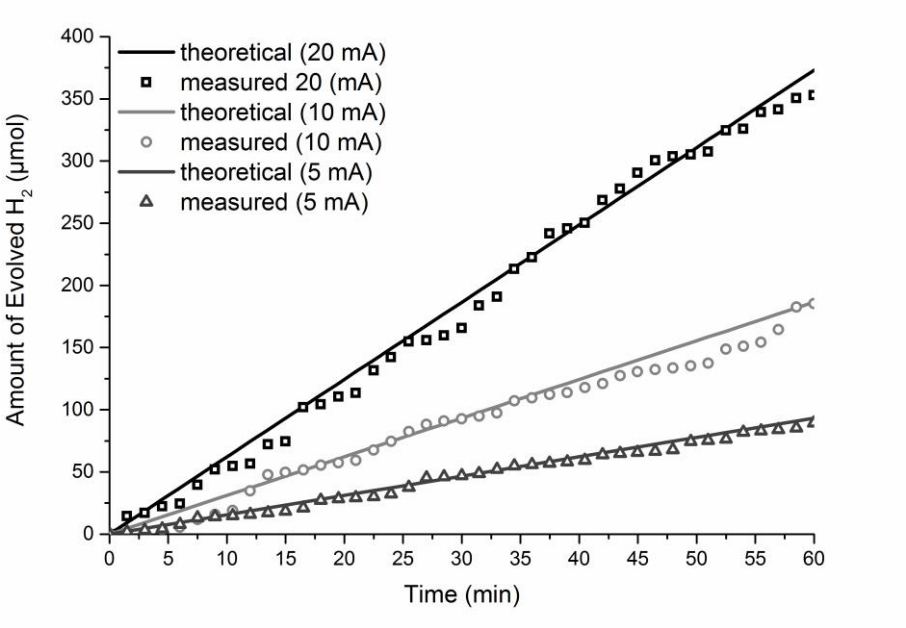

Supplementary Figure 8. Calculated (lines) versus real (markers) hydrogen production using patterned Si microwire photocathode, biased at 5, 10 or 20 mA. Microwire array with 6 µm pitch, upper 2 µm functionalized with Ni-Mo (180 s deposition). The used setup to measure the activity is given in Supplementary Figure 3c. The H_2 production for patterned Ni-Mo (180 s) Si microwire samples b in Figure 3b was measured by gas chromatography (GC). Here, the n^+/p junction was biased by contacting the emitter of the Si microwire photocathode and applying a bias to generate either 5, 10 or 20 mA of current output. The calculated and measured produced H_2 amounts match excellently, indicating a nearly 100% Faradaic efficiency.

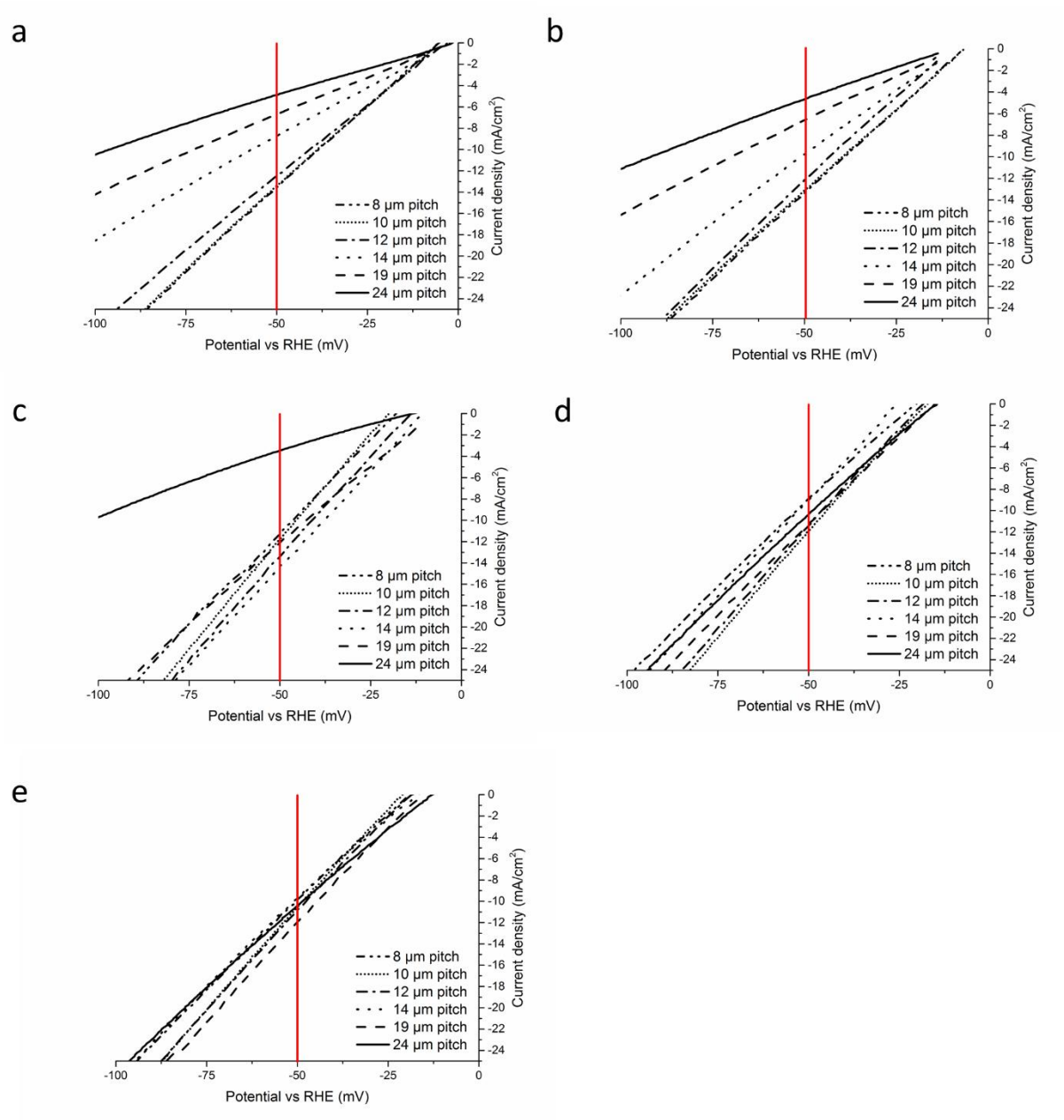

Supplementary Figure 9. Plots of current density *vs.* potential, obtained for Si microwire arrays with different pitch as stated in the legends and the upper (**a**) 2 µm (**b**) 9 µm, (**c**) 17 µm, (**d**) 25 µm and (**e**) 36 µm functionalized with Ni-Mo. Scans were performed in the dark in an electrochemical cell, containing a 0.1 M H_2SO_4 solution. The used setup to measure the activity is given in Supplementary Figure 3d.

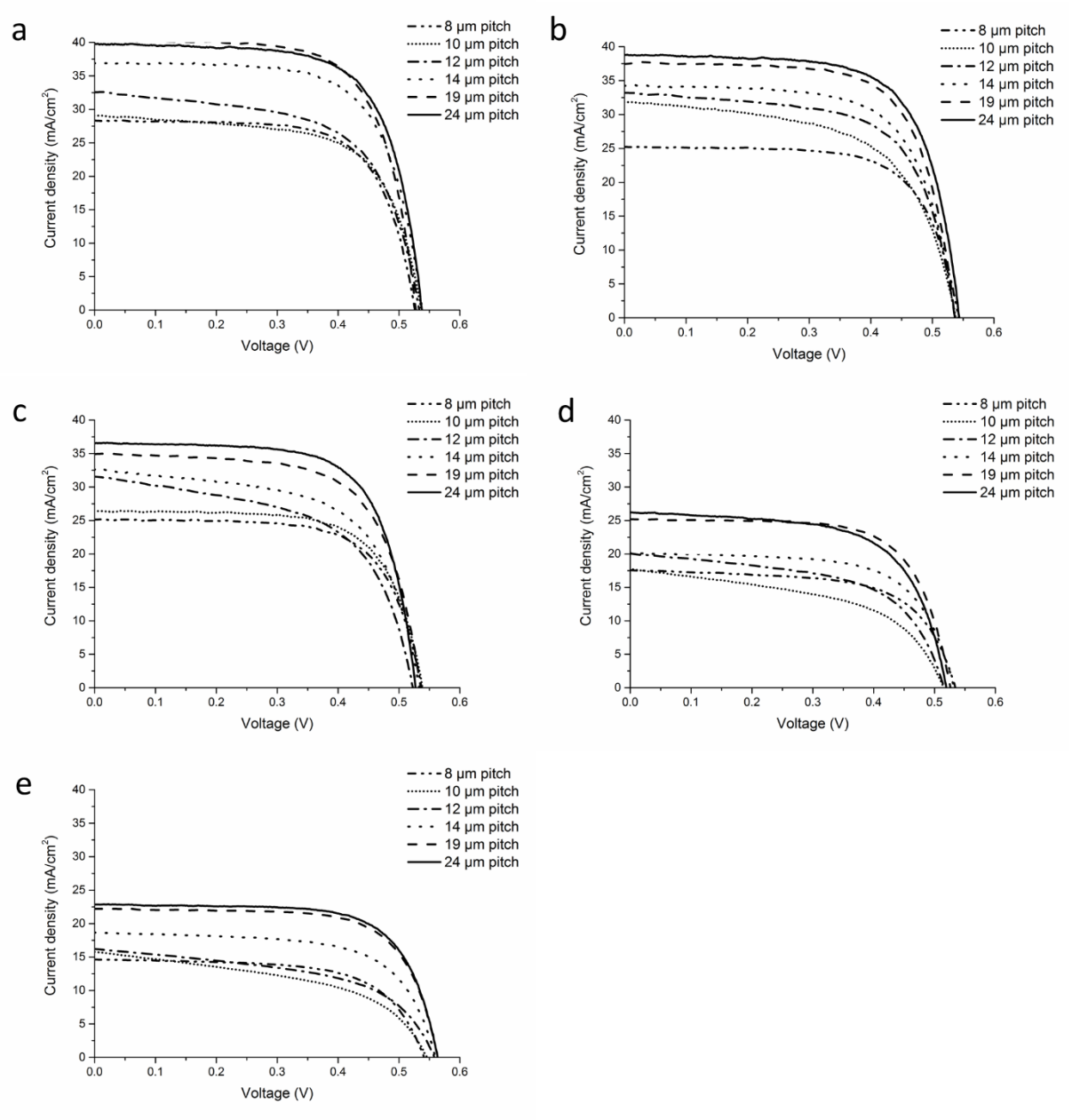

Supplementary Figure 10. *JV* measurements of microwire substrates for different pitches as stated in the legends and the upper (**a**) 2 µm (**b**) 9 µm, (**c**) 18 µm, (**d**) 25 µm and (**e**) 35 µm functionalized with Ni-Mo. Each line is the average of two different samples prepared with the same settings. The used setup to measure the activity is given in Supplementary Figure 3b.

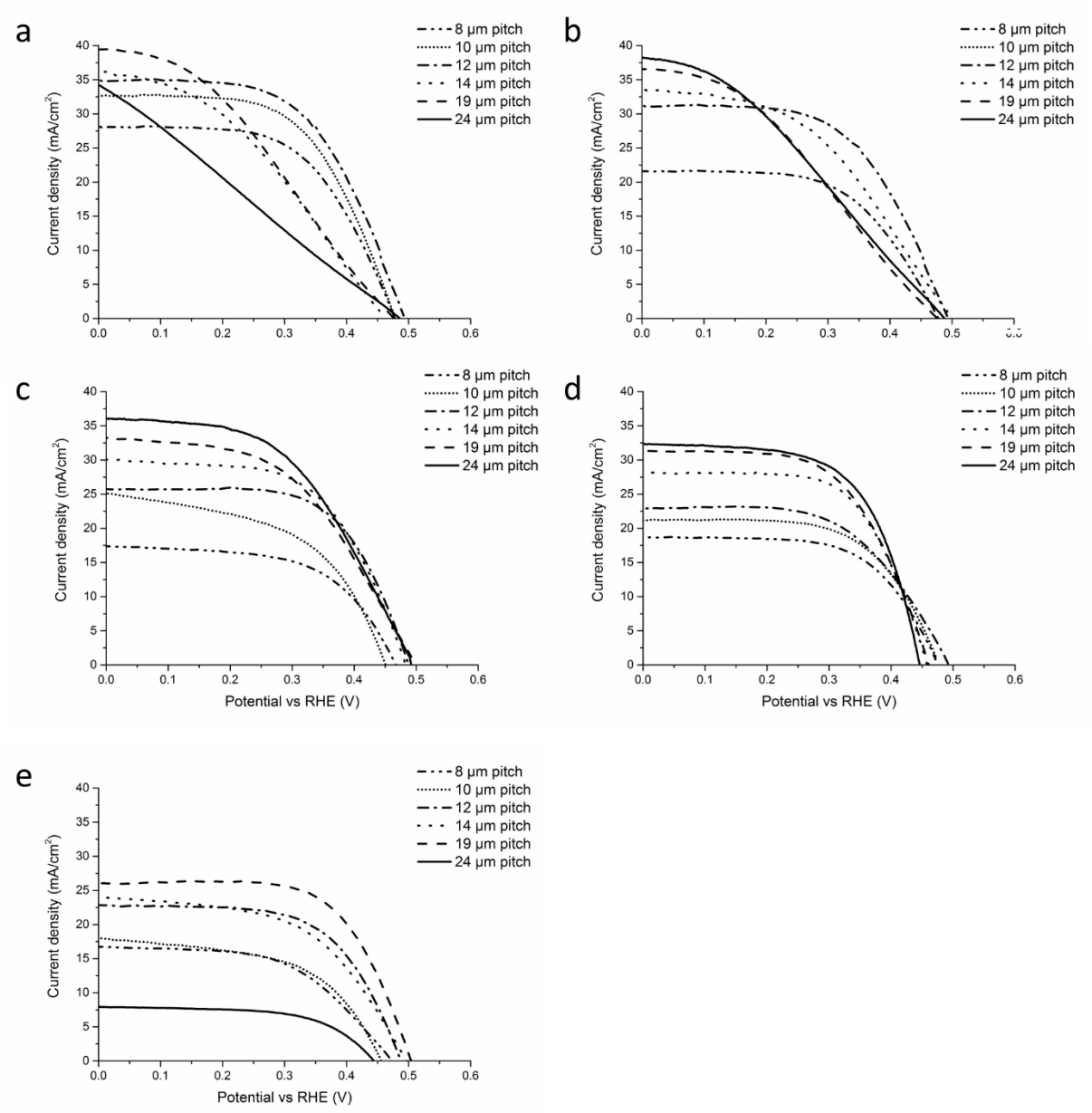

Supplementary Figure 11. *JE* measurements of microwire substrates for different pitches as indicated and the upper (**a**) 2 µm (**b**) 9 µm, (**c**) 17 µm, (**d**) 25 µm and (**e**) 35 µm functionalized with Ni-Mo. Each line is the average of two different samples prepared with the same settings. The used setup to measure the activity is given in Supplementary Figure 3c.

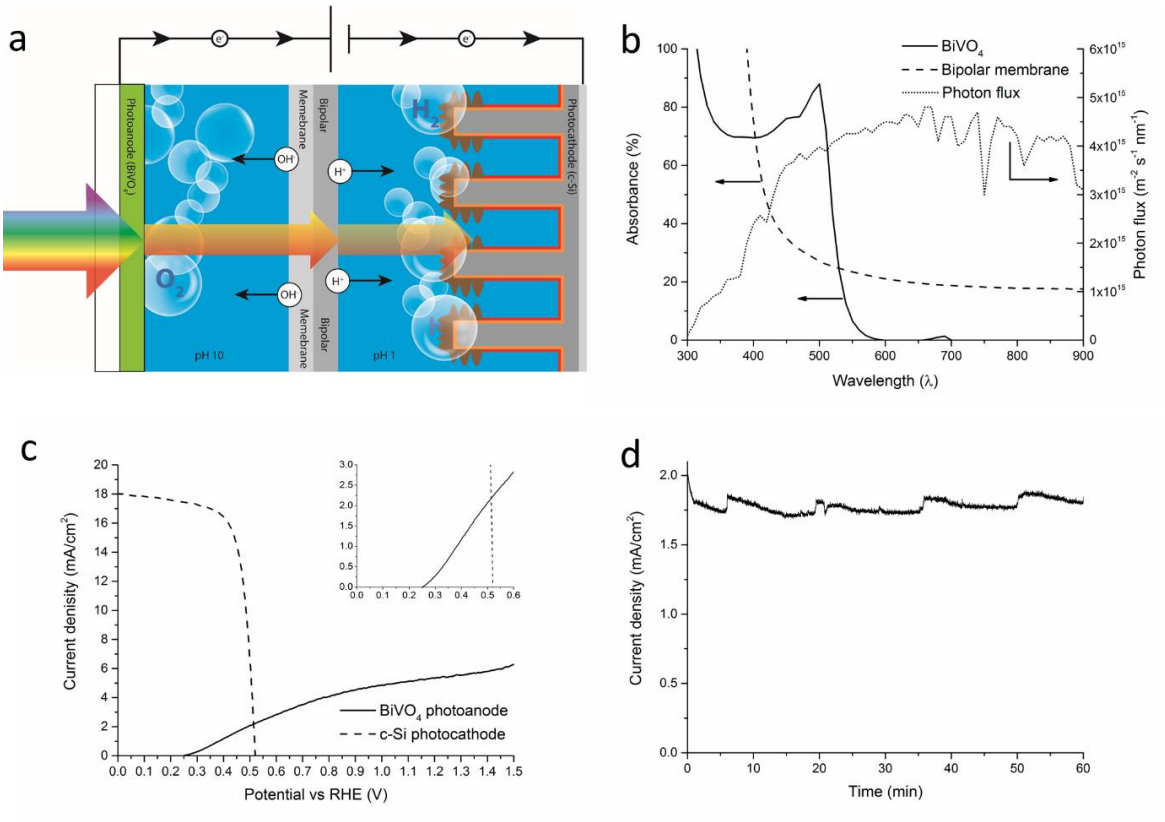

Supplementary Figure 12. (**a**) Schematic setup for a full S2F device with the different absorbances and losses in light through every layer. (**b**) Absorbance spectra of the $BiVO_4$ layer (solid line) and the employed bipolar membrane (dashed line). The AM 1.5G photon flux spectrum (dotted line) is shown as well. (**c**) Current density (J_{ph}) *vs.* potential (vs. RHE, (*V*)) for the Si microwire photocathode and the $BiVO_4$ photoanode. The inset shows a section of the same graph magnified around the operating point. (**d**) Stability of unbiased water splitting (at 0.0 V versus counter electrode) over the course of an hour.

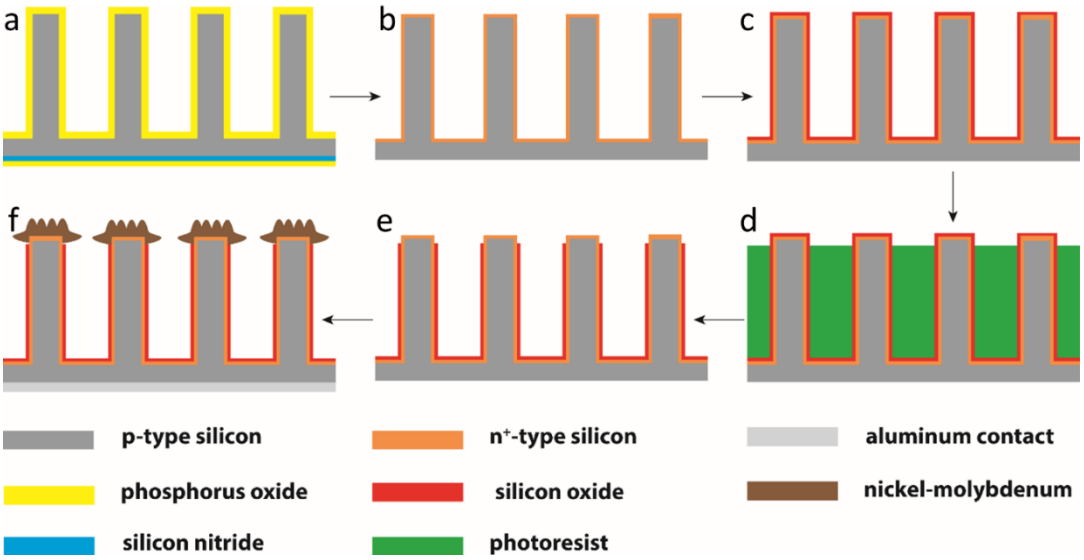

Supplementary Figure 13. Schematic fabrication process: (**a**) Wire array obtained after deep reactive ion etching of a silicon wafer with a photoresist pattern on the front side and silicon-rich silicon nitride on the backside, followed by the deposition of the dopant oxide by LPCVD (phosphorus). (**b**) Formation of the radial junction, by a drive-in step at 1050 °C for 15 min. (**c**) Deposition of a passivation layer of SiO_2 by LPCVD. (**d**) Filling of the wire arrays with photoresist, followed by controlled retraction by O_2 plasma. (**e**) Selective removal of the passivation layer by BHF wet etching. (**f**) Deposition of aluminum back contacts by sputtering and of the catalyst by electrodeposition.

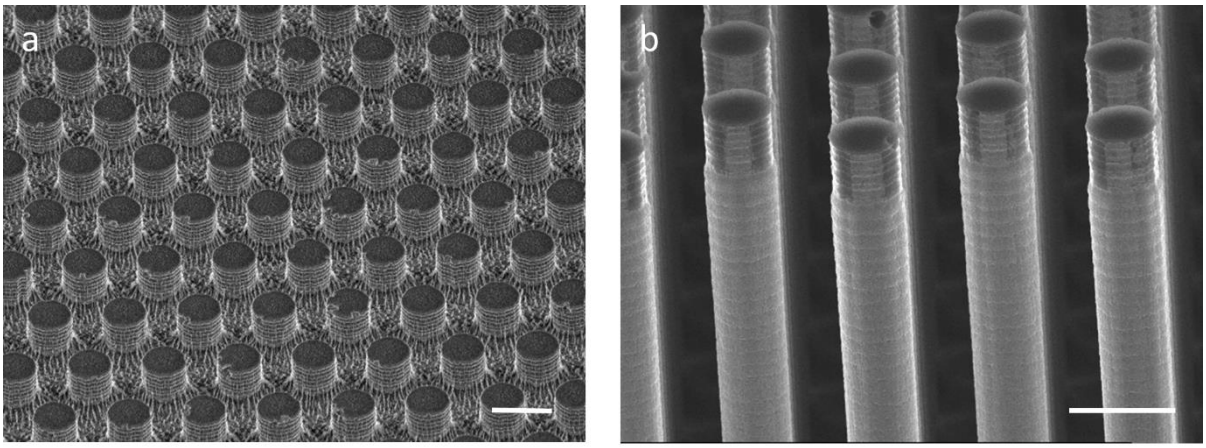

Supplementary Figure 14. (**a**) HR-SEM images of Si microwire arrays with photoresist between the microwires, which is etched by O2 plasma. (**b**) Si microwire array with selectively removed SiO2 from the tops by etching (a) in BHF. Scale bar is 5 µm

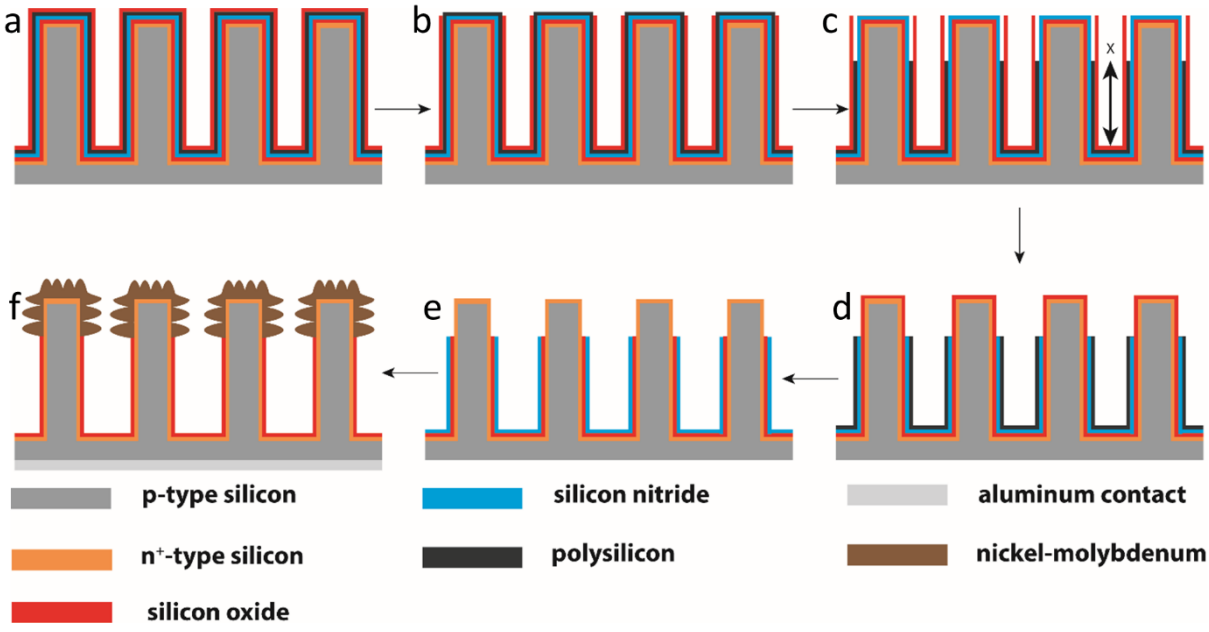

Supplementary Figure 15. Schematic outline of the process for spatioselective formation of a passivation layer and deposition of the catalyst. (**a**) On the radially doped silicon microwires several layers are formed by LPCVD: silicon oxide, silicon nitride, and polysilicon. The outer part of the polysilicon is then thermally oxidized. (**b**) The thermal silicon oxide is opened at the top by inclined ion beam etching. (**c**) the polysilicon layer is retracted in hot TMAH solution to the desired height (x). (**d**) The thermal silicon oxide is removed in buffered HF solution, and the silicon nitride is etched in hot phosphoric acid solution. (e) The polysilicon is stripped in hot TMAH solution, and the LPCVD silicon oxide is etched in buffered HF solution. (**e**) The silicon nitride is stripped in hot phosphoric acid solution, and (**f**) electrical back side contact is formed by sputtering aluminum, and finally the catalyst is deposited selectively by electrodeposition.

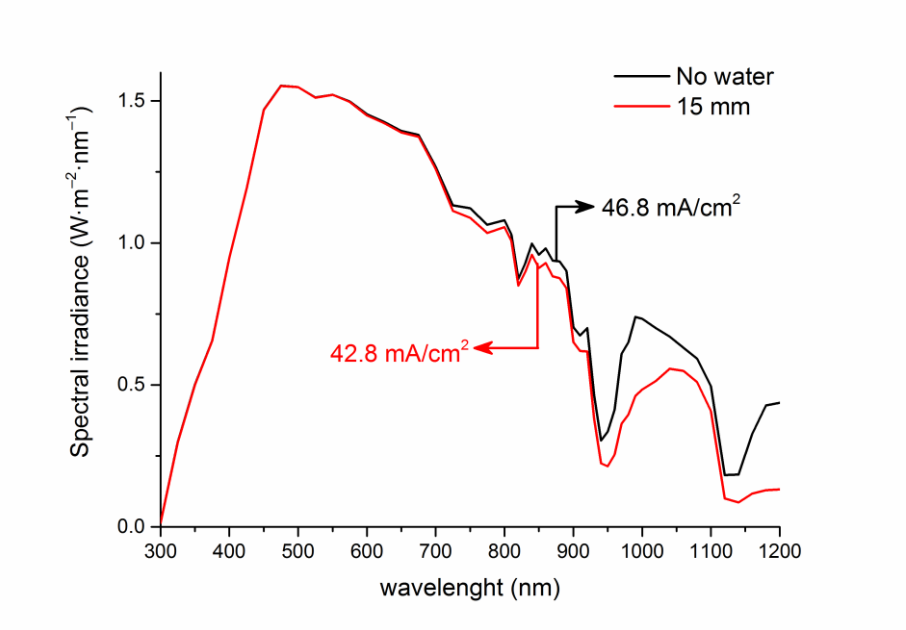

Supplementary Figure 16. Plot of the ASTM reference pattern (black) and calculated transmittance through 15 mm of water (red). Each graph was integrated in the range of 300 to 1200 nm to calculate the maximum photo-current.

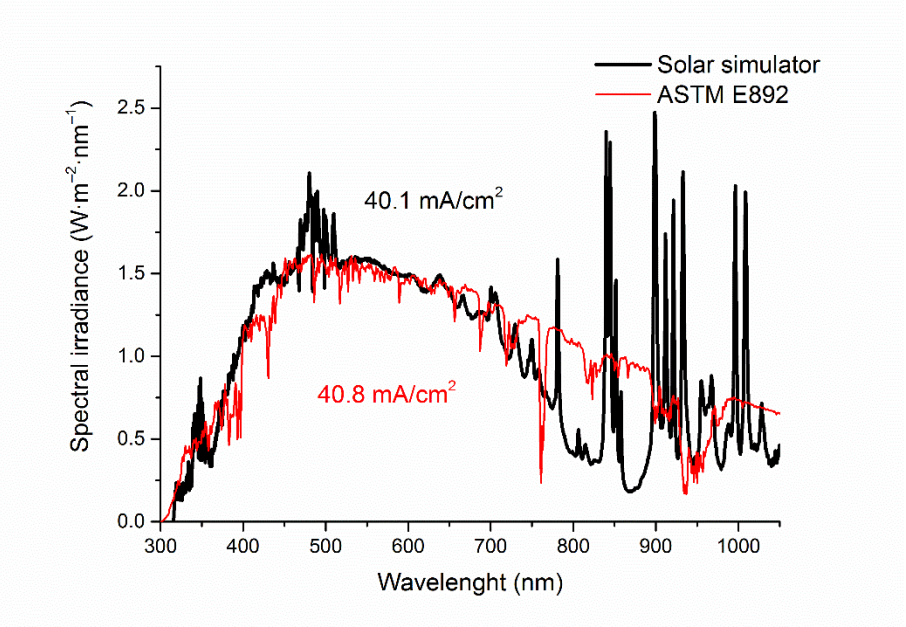

Supplementary Figure 17. Spectral irradiance plot of an ASTM reference pattern (red) and of the solar simulator used for the measurements in this paper (black).

Supplementary Tables

Supplementary Table 1. *JV* characteristics for the Si micropillar arrays with radial n^+/p-junctions, without or with Ni-Mo as catalyst, as determined from the *JV* graphs shown in Figure 2

Route	Device	Deposition time (s)	V_{oc} (V)	J_{sc} (mA/cm^2)	*FF* (%)	η (%)
a	Bare Si	--	0.46	37.6	65	11.1
	Ni-Mo (10 s)	10	0.46	35.5	64	10.3
	Ni-Mo (15 s)	15	0.46	32.8	64	9.7
	Ni-Mo (30 s)	30	0.46	29.4	60	8.0
	Ni-Mo (180 s)	180	0.44	4.2	63	1.1
b	Bare Si	--	0.53	41.7	60	13.0
	Ni-Mo (180 s)	180	0.52	28.3	65	9.6

Supplementary Table 2. *JE* characteristics for the Si micropillar arrays with radial n^+/p-junctions, with Ni-Mo or Pt as catalyst, as determined from the *JE* graphs shown in Figure 3. The values of *FF,* V_{OC} and J_{ph} are referenced to the equilibrium potential of the half-reaction being performed at the photocathode.

Route	Device	Deposition time (s)	V_{oc} (V)	J_{ph} (mA/cm^2)	*FF* (%)	Plateau J_{ph} * (mA/cm^2)	η_{IRC} (%)
a	Ni-Mo (10 s)	10	0.28	16.7	13	36	0.58
	Ni-Mo (15 s)	15	0.30	16.5	12	32	0.57
	Ni-Mo (30 s)	30	0.31	15.1	11	29	0.51
	Ni-Mo (180 s)	180	0.46	2.7	45	3.0	1.04
b	Ni-Mo	180	0.48	29.1	47	32	6.79
	Pt	30	0.48	30.4	51	31	7.06

* Plateau current density measured at -0.5 V vs RHE of Figure 3a/b

Supplementary Table 3. Cell characteristics from Supplementary Figure 9 and 10 for various pitches and catalyst coverages. R_s was obtained by linearizing the data series (resulting slope = $1/R_s$) of the catalytic activity of Supplementary Figure 9, between 0 and 50 mV vs. RHE. The calculated FF_s values were obtained using the analytical expression developed by Green *et al*.[5] Resistances from only the PV behavior, as determined by taking the slopes (=$1/R$) in the graphs of Supplementary Figure 10 at V_{oc}, gave almost constant, and significantly smaller values (0.77-0.83 Ω/cm^2) than the R_s values reported in the table.

			2 um			
	8 µm	**10 µm**	**12 µm**	**14 µm**	**19 µm**	**24 µm**
V_{oc} **(V)**	0.48	0.48	0.49	0.49	0.48	0.49
I_{sc} **(mA/cm^2)**	28.99	33.54	35.55	37.33	40.84	41.28
R_s **(Ω/cm^2)**	3.67	3.71	3.98	5.73	7.43	10.26
FF **(--)**	60.69	59.33	62.32	43.18	37.67	35.86
FF_s **(--)**	61.20	58.20	59.37	45.37	35.36	31.52
			9 um			
V_{oc} **(V)**	0.48	0.49	0.49	0.49	0.48	0.49
I_{sc} **(mA/cm^2)**	21.63	25.44	31.11	33.52	36.57	38.26
R_s **(Ω/cm^2)**	3.72	3.79	4.89	5.07	7.47	10.57
FF **(--)**	57.88	59.02	57.50	46.20	35.93	33.19
FF_s **(--)**	60.87	60.06	59.73	46.39	36.33	36.50
			17 um			
V_{oc} **(V)**	0.47	0.45	0.49	0.48	0.49	0.49
I_{sc} **(mA/cm^2)**	17.27	24.43	25.69	29.80	33.05	35.85
R_s **(Ω/cm^2)**	4.50	4.16	3.75	2.78	4.14	4.42
FF **(--)**	58.25	52.54	63.29	58.69	50.52	50.68
FF_s **(--)**	65.45	50.25	63.37	60.42	50.11	50.72
			22 um			
V_{oc} **(V)**	0.47	0.47	0.49	0.46	0.46	0.45
I_{sc} **(mA/cm^2)**	18.71	21.23	22.96	28.00	31.23	32.17
R_s **(Ω/cm^2)**	5.54	4.20	4.38	3.38	4.37	4.82
FF **(--)**	62.38	62.15	57.33	63.61	59.14	62.18
FF_s **(--)**	61.27	63.73	62.92	62.00	59.05	60.87
			35 um			
V_{oc} **(V)**	0.47	0.46	0.49	0.50	0.50	0.44
I_{sc} **(mA/cm^2)**	16.59	17.62	22.71	23.72	25.98	7.87
R_s **(Ω/cm^2)**	5.02	4.70	4.62	4.96	4.20	4.75
FF **(--)**	54.66	55.62	61.75	53.96	64.91	60.67
FF_s **(--)**	62.01	60.99	58.50	56.63	58.71	60.22

Supplementary Table 4. A survey of micro- and nanowire H_2 producing half cells. Measurements done under AM 1.5G in their best performing electrolyte.

Configuration	V_{oc} (mV)	J_{ph} (mA/cm^2)	FF (%)	η_{IRC} (%)	ref
		Ni-Mo			
n$^+$/p-Si MWs	**480**	**34.9**	**62**	**10.8**	**This work**
n$^+$/p-Si MWs	420	14.3	48	2.9	[6]
n$^+$/p-Si MWs	485	10.3	45	2.2	[7]
n$^+$/p-Si MWs	349	13.5	12	0.6	[8]
p$^+$-Si MWs	145	7.0	35	0.4	[9]
		Pt			
n$^+$/p-Si MWs	**480**	**36.5**	**48**	**7.1**	**This work**
n$^+$/p-Si MWs	540	15.0	71	5.8	[10]
n$^+$/p-Si MWs	510	20.2	49	5.0	[6]
n$^+$/p-Si MWs	440	14.0	46	2.8	[11]
n$^+$/p-Si MWs	441	13.2	47	2.7	[7]
p-Si NWs	380	21.2	30	2.5	[12]
n$^+$/p-Si MWs	330	15.0	30	1.5	[13]
p-Si NWs	420	19.9	45*	3.8	[14]
p-Si NWs	370	16.5	44	2.6	[15]
p-si NWs	310	29.2	26*	2.4	[16]
p-Si NWs	280	19.6	17	1.6	[17]
p-Si NWs	310	9.0	55	1.5	[18]
p-Si NWs	250	20.7	25*	1.3	[19]
p-Si MWs	480	12.8	20*	1.2	[20]
p$^+$-Si MWs	265	11.7	31	1.0	[9]
		Other			
p-Si NWs/$N_{12}P_5$	400	21.0	36	3.0	[21]
p-Si NWs/CoP	407	15.6	27	2.9	[17]
p-Si NWs/FeP	470	13.9	45	2.8	[22]
p-Si NWs/$NiCoSe_x$	250	37.5	26*	2.5	[16]
p-Si NWs/NiB	440	15.6	36	2.5	[12]
p-Si NWs/CoB	450	19.5	29	2.5	[12]
p-Si NW/N-GQS	210	35.0	32	2.3	[23]
p-Si NWs/MoS_3	360	24.9	28*	2.3	[15]

p-Si NWs/a-WS_3	400	19.0	30*	2.0	[24]
n^+/p-Si MWs/CoP	480	17.0	24	1.9	[11]
n^+/p-Si MWs/MoS_2	300	15.0	30	1.4	[13]
p-Si MWs/Mo_3S_4	150	9.3	--	1.2	[25]
p-Si NWs/$NiSe_x$	225	20.5	26*	1.2	[16]
p-Si MWs/$CoMoS_x$	192	17.2	23	0.7	[16]
p-Si NWs/$CoSe_x$	140	15.3	26*	0.6	[16]
p-Si MWs/$CoSe_2$	200	9.0	25*	0.5	[26]
p-Si MWs/C_3N_4/$CoSe_2$	195	4.9	25*	0.2	[27]

* estimated from figures from reference

Supplementary Table 5. Deposition time of Ni-Mo catalyst on microwire arrays for every microwire pitch/coverage combination. Here, f_c is the filling fraction, in order to give a quick comparison with the results of Chen *et al.*[4] The geometric filling fraction in the study of Chen *et al.* is defined as the ratio of the geometric area of the catalyst to the total geometric area of the photoelectrode. Therefore, f_c is directly related to the pitch of the our Si microwires when only the tops of the microwires with a spatioselective catalyst are taken into account. D_t is the deposition time for every chosen pitch and coverage height, *i.e.* 2, 9, 18, 22, and 35 µm. The HER catalytic activity of Ni-Mo was essentially unchanged when the nominal deposition time was >180 s for microwire arrays with a pitch of 8 µm and the top 2 µm covered with Ni-Mo, as is seen from Supplementary Figure 4. The deposition time for each sample in this study was corrected for absolute surface area of exposed silicon. In that way it was tried to achieve approximately the same catalyst layer thickness in all cases.

Pitch	f_c **(%)**	D_t **(s) 2 µm**	D_t **(s) 9 µm**	D_t **(s) 18 µm**	D_t **(s) 22 µm**	D_t **(s) 35 µm**
8	22.7	180	270	540	630	1080
10	14.5	65	195	390	455	780
12	10.1	45	135	270	315	540
14	7.4	33	99	198	231	396
19	4.0	18	54	108	126	216
24	2.5	12	36	72	84	144

Supplementary Discussion

We have fabricated a full S2F device, by combining a backside-illuminated photoanode ($BiVO_4$) and a frontside-illuminated photocathode (c-Si) in combination with a bipolar membrane, as seen Supplementary Figure 12a**.**

Part of the light illuminated at the backside of the photoanode is absorbed by the $BiVO_4$ film and by the bipolar membrane, and the remaining light is available for the c-Si microwire array photocathode. We performed UV-Vis absorbance measurements to investigate the wavelength dependence of absorption in both materials (see Supplementary Figure 12b). $BiVO_4$ has a strong absorption in the region of 300 to 520 nm, which is expected for a material with indirect and direct bandgaps of 2.6 eV and 2.4 eV, respectively. An overlay with the used photon flux is made, and $BiVO_4$ only uses a fraction of the solar spectrum. Our employed bipolar membrane has a strong absorption for wavelengths <500 nm, although the majority of these photons are already absorbed in a complete S2F device by the $BiVO_4$ layer (see Supplementary Figure 12b). The absorption rapidly decreases with increasing wavelengths, and the membrane shows ~15% absorbance for wavelengths >600 nm. The maximum photon current generated by a frontside-illuminated c-Si photocathode, after subtracting the absorption of the $BiVO_4$ layer (~6.5 mA/cm^2) and bipolar membrane (~9 mA/cm^2) is 29 mA/cm^2 in the range of 300 to 1100 nm. The latter is for maximum absorbance within the c-Si microwires and without influence of the catalyst on top of the c-Si microwires.

The performance of the photoanode and –cathode were evaluated independently from each other under one sun illumination, as seen in Supplementary Figure 12c. The photoanode performance is comparable with the performance reported by Kim *et al.*[28] The performance of the photocathode was assessed with the $BiVO_4$ photoanode and a bipolar membrane in front of the c-Si photocathode. A clear decrease in photocurrent is observed for the photocathode when compared with the values reported in the main text, but this is understandable seen the photocurrent losses induced by the two overlayers (*i.e.* $BiVO_4$ and the membrane). The plot in Supplementary Figure 12c shows the crossover point for unbiased water splitting and an inset highlights this point at ~513 mV *vs.* RHE. It indicates that the resulting unbiased performance is primarily limited by the performance of the $BiVO_4$ photoanode,.

By employing a bipolar membrane, both the photoanode and –cathode can be operated at their preferred pH, as demonstrated by Vermaas *et al.*[29] The stability of the setup in Supplementary Figure 12a was assessed in Supplementary Figure 12d, by measuring the photocurrent under open circuit potential (0.0 V versus counter electrode). Steps are visible within the measured data, which are most likely due to bubble formation and release within the cell and temporary blocking the incoming light.

Supplementary References

1 Chen, Y., Shen, J. & Chen, N. X. The effect of Mo atoms in ternary nitrides with eta-type structure. *Solid State Commun.* **149**, 121-125 (2009).

2 Suzuki, T., Ochisi, S. & Mishima, Y. Lattice paramaters of Ni (y), Ni3 Al (y), and Ni3 Ga (y) solid solutions with the addition of transition B-subgroup elements. *Bulletin of Research Laboratory of Precision Machinery and Electronics, Tokio Inst. Technol* **1**, 15-28 (1984).

3 McKone, J. R., Sadtler, B. F., Werlang, C. A., Lewis, N. S. & Gray, H. B. Ni-Mo Nanopowders for Efficient Electrochemical Hydrogen Evolution. *ACS Cat.* **3**, 166-169 (2013).

4 Chen, Y. K., Sun, K., Audesirk, H., Xiang, C. X. & Lewis, N. S. A quantitative analysis of the efficiency of solar-driven water-splitting device designs based on tandem photoabsorbers patterned with islands of metallic electrocatalysts. *Energy Environ. Sci.* **8**, 1736-1747 (2015).

5 Green, M. A. Accuracy of analytical expressions for solar cell fill factors. *Solar Cells* **7**, 337-340 (1982).

6 Shaner, M. R., McKone, J. R., Gray, H. B. & Lewis, N. S. Functional integration of Ni-Mo electrocatalysts with Si microwire array photocathodes to simultaneously achieve high fill factors and light-limited photocurrent densities for solar-driven hydrogen evolution. *Energy Environ. Sci.* **8**, 2977-2984 (2015).

7 Warren, E. L., McKone, J. R., Atwater, H. A., Gray, H. B. & Lewis, N. S. Hydrogen-evolution characteristics of Ni-Mo-coated, radial junction, n+p-silicon microwire array photocathodes. *Energy Environ. Sci.* **5**, 9653-9661 (2012).

8 Huang, Z. *et al.* Comparison between the measured and modeled hydrogen-evolution activity of Ni- or Pt-coated silicon photocathodes. *Int. J. Hydrogen Energy* **39**, 16220-16226 (2014).

9 McKone, J. R. *et al.* Evaluation of Pt, Ni, and Ni-Mo electrocatalysts for hydrogen evolution on crystalline Si electrodes. *Energy Environ. Sci.* **4**, 3573-3583 (2011).

10 Boettcher, S. W. *et al.* Photoelectrochemical hydrogen evolution using Si microwire arrays. *J. Am. Chem. Soc.* **133**, 1216-1219 (2011).

11 Roske, C. W. *et al.* Comparison of the Performance of CoP-Coated and Pt-Coated Radial Junction n^+p-Silicon Microwire-Array Photocathodes for the Sunlight-Driven Reduction of Water to H_2(g). *J. Phys. Chem. Lett.* **6**, 1679-1683 (2015).

12 Yang, Y. *et al.* Evident Enhancement of Photoelectrochemical Hydrogen Production by Electroless Deposition of M-B (M = Ni, Co) Catalysts on Silicon Nanowire Arrays. *ACS Appl. Mater. Interfaces* **8**, 30143-30151 (2016).

13 Zhang, L., Liu, C., Wong, A. B., Resasco, J. & Yang, P. MoS_2-wrapped silicon nanowires for photoelectrochemical water reduction. *Nano Res.* **8**, 281-287 (2015).

14 Oh, I., Kye, J. & Hwang, S. Enhanced Photoelectrochemical Hydrogen Production from Silicon Nanowire Array Photocathode. *Nano Lett.* **12**, 298-302 (2012).

15 Huang, Z. *et al.* Enhanced photoelectrochemical hydrogen production using silicon nanowires@MoS_3. *Nano Energy* **2**, 1337-1346 (2013).

16 Zhang, H. *et al.* A p-Si/$NiCoSe_x$ core/shell nanopillar array photocathode for enhanced photoelectrochemical hydrogen production. *Energy Environ. Sci.* **9**, 3113-3119 (2016).

17 Bao, X. Q., Fatima Cerqueira, M., Alpuim, P. & Liu, L. Silicon nanowire arrays coupled with cobalt phosphide spheres as low-cost photocathodes for efficient solar hydrogen evolution. *Chem. Commun.* **51**, 10742-10745 (2015).

18 Dai, P. *et al.* Solar Hydrogen Generation by Silicon Nanowires Modified with Platinum Nanoparticle Catalysts by Atomic Layer Deposition. *Angew. Chem. Int. Ed.* **52**, 11119-11123 (2013).

19 Dasgupta, N. P., Liu, C., Andrews, S., Prinz, F. B. & Yang, P. Atomic Layer Deposition of Platinum Catalysts on Nanowire Surfaces for Photoelectrochemical Water Reduction. *J. Am. Chem. Soc.* **135**, 12932-12935 (2013).

20 Sim, U., Jeong, H.-Y., Yang, T.-Y. & Nam, K. T. Nanostructural dependence of hydrogen production in silicon photocathodes. *J. Mat. Chem. A* **1**, 5414-5422 (2013).

21 Huang, Z. *et al.* $Ni_{12}P_5$ Nanoparticles as an Efficient Catalyst for Hydrogen Generation via Electrolysis and Photoelectrolysis. *ACS Nano* **8**, 8121-8129 (2014).
22 Lv, C. *et al.* Silicon nanowires loaded with iron phosphide for effective solar-driven hydrogen production. *J. Mat. Chem. A* **3**, 17669-17675 (2015).
23 Sim, U. *et al.* N-doped graphene quantum sheets on silicon nanowire photocathodes for hydrogen production. *Energy Environ. Sci.* **8**, 1329-1338 (2015).
24 Huang, Z. *et al.* Tungsten Sulfide Enhancing Solar-Driven Hydrogen Production from Silicon Nanowires. *ACS Appl. Mater. Interfaces* **6**, 10408-10414 (2014).
25 Hou, Y. *et al.* Bioinspired molecular co-catalysts bonded to a silicon photocathode for solar hydrogen evolution. *Nat Mater* **10**, 434-438 (2011).
26 Basu, M. *et al.* Heterostructure of Si and $CoSe_2$: A Promising Photocathode Based on a Non-noble Metal Catalyst for Photoelectrochemical Hydrogen Evolution. *Angew. Chem. Int. Ed.* **54**, 6211-6216 (2015).
27 Basu, M. *et al.* $CoSe_2$ Embedded in C_3N_4: An Efficient Photocathode for Photoelectrochemical Water Splitting. *ACS Appl. Mater. Interfaces* **8**, 26690-26696 (2016).
28 Kim, J. H. *et al.* Hetero-type dual photoanodes for unbiased solar water splitting with extended light harvesting. *Nat. Commun.* **7**, 13380 (2016).
29 Vermaas, D. A., Sassenburg, M. & Smith, W. A. Photo-assisted water splitting with bipolar membrane induced pH gradients for practical solar fuel devices. *J. Mat. Chem. A* **3**, 19556-19562 (2015).